EES Solar

Accepted Manuscript

This article can be cited before page numbers have been issued, to do this please use: M. Hossain, C. J. Dolan, E. Oberholtz, D. Kamiyama, J. Palmer, P. E. Marchezi, T. Kodalle, C. M. Sutter-Fella and D. P. Fenning, *EES Sol.*, 2026, DOI: 10.1039/D6EL00041J.

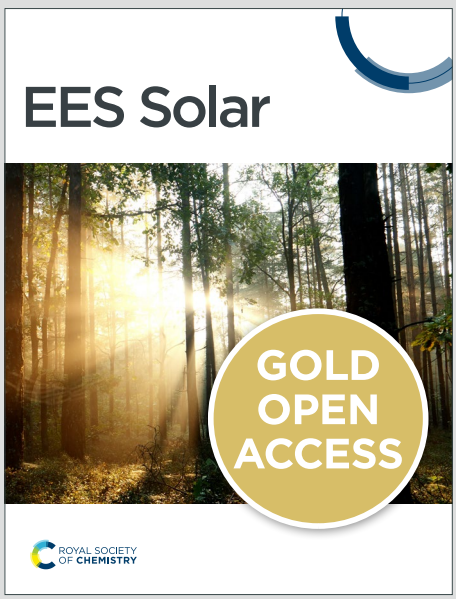

View Article Online
DOI: 10.1039/D6EL00041J

Broader context statement

The transition of halide perovskite solar cells from laboratory to commercial production demands scalable deposition processes compatible with real-world manufacturing environments. Lab-scale fabrication has largely relied on antisolvent-assisted deposition under inert atmospheres, conditions that are costly and impractical to replicate at industrial scale. Antisolvent-free ambient processing offers a compelling alternative, yet its adoption requires understanding how the deposition environment governs crystallization and ultimately film and device quality. This work provides that mechanistic insight, revealing how ambient conditions can be systematically tuned to replicate inert synthesis outcomes without sacrificing performance. The results highlight the critical role of controlled humidity in directing antisolvent-free perovskite crystallization pathways, establishing a practical framework for transferring processes from inert to ambient conditions and accelerating the path toward scalable, commercially viable perovskite solar technology.

View Article Online
DOI: 10.1039/D6EL00041J

ARTICLE

Balancing Moisture and Oxygen Can Match the Crystallization Dynamics of Inert Halide Perovskite Processing

Received 00th January 20xx,
Accepted 00th January 20xx

DOI: 10.1039/x0xx00000x

Maimur Hossain[a], Connor J. Dolan[a], Eric Oberholtz[a], Darya Kamiyama[a], Jack R. Palmer[a], Paulo E. Marchezi[a], Tim Kodalle[c,d], Carolin M. Sutter-Fella[c], David P. Fenning[a,b]

Understanding crystallization in ambient environments is essential for scaling the fabrication of halide perovskite solar cells. Antisolvent-free perovskite deposition offers improved compatibility with high-throughput processing but introduces distinct crystallization dynamics relative to the more ubiquitous use of antisolvents in lab-scale perovskite fabrication. These dynamics are driven by interactions between solutes, solvent and the deposition environment. Using *in situ* wide-angle X-ray scattering during spin-coating and annealing, we demonstrate how relative humidity (RH) and oxygen, can be tuned to drive polytype evolution during ambient crystallization of formamidinium lead iodide to match that of inert synthesis and achieve comparable film and device quality. In an inert (N_2) environment, we find that perovskite films follow a well-established 2H → 3C phase transformation with a small period of coexistence of the 4H and 6H phase during heating. During crystallization in dry air (RH 0%), the added presence of oxygen leads to the dominance of 4H intermediate for an extended duration, establishing a 2H → 4H → 3C pathway. Introducing low humidity (RH 10%) suppresses the 4H phase to a short-lived intermediate above 100 °C, facilitating a more direct transition to the desired 3C phase and almost replicating the crystallization behavior observed under inert conditions. Interestingly, films crystallized under RH 10% show a lower onset temperature for the perovskite 3C phase than under N_2. At higher humidity (RH 40%), the strong interaction of oxygen and moisture with iodoplumbates appears to stabilize higher order polytypes (4H and 6H). Devices fabricated under RH 10% achieve higher efficiency and enhanced stability compared to those produced in inert atmosphere. These findings provide mechanistic insight into crystallization pathways in different environments and provide a framework to transfer processes from inert to ambient conditions. The results highlight the critical role of controlled humidity in tuning antisolvent-free perovskite crystallization for scalable processing.

Introduction

Despite achieving impressive power conversion efficiency (PCE) >27% in laboratory settings, perovskite solar cells (PSCs) remain hindered by scalability and durability concerns in commercial production.[1,4] Formamidinium lead triiodide ($FAPbI_3$) stands out as the most promising candidate, with a band gap of 1.48 eV, better thermal stability than methylammonium variants, and excellent charge transport.[5,6] Yet upscaling $FAPbI_3$ to commercial production requires moving beyond current lab-based methods toward manufacturing-compatible processes.[7-9] Conventional perovskite processing via spin coating relies heavily on antisolvent dripping to induce rapid nucleation and crystallization. While effective in laboratory settings, antisolvent-based approaches are fundamentally limited in scalability and reproducibility, particularly for large-area or roll-to-roll deposition techniques required for commercial manufacturing.[10,11] Antisolvent-free (ASF) methods offer a compelling alternative for high-throughput production by eliminating the need for precise antisolvent timing and enabling continuous processing.[12–14]

Methylammonium chloride (MACl) functions as a crucial volatile additive, promoting $FAPbI_3$ crystallization via cubic templating and $[PbI_6]^{4-}$ skeleton stabilization during intermediate phase formation.[15–17] However, residual MACl in the annealed film can compromise long-term device stability due to weaker thermal stability of MA^+ and the reactive nature of MA^0 with FA^+ to form n-methyl formamidinium, which is detrimental for long term stability.[14,18,19]

Utilizing moisture in a controlled humidity environment during crystallization offers a potential solution to remove MA from the final film. Moisture promotes MA^+ deprotonation and subsequent MA^0 and HCl volatilization, which regulates the

[a] Aiiso Yufeng Li Family Department of Chemical and Nano Engineering, University of California San Diego, 9500 Gilman Drive, La Jolla, California 92093, United States.
[b] Materials Science & Engineering Program, University of California San Diego, 9500 Gilman Drive, La Jolla, California 92093, United States
[c] Molecular Foundry Division, Lawrence Berkeley National Laboratory, 1 Cyclotron Road, Berkeley, California 94710, United States.
[d] Advanced Light Source, Lawrence Berkeley National Laboratory, 1 Cyclotron Road, Berkeley, California 94710, United States.

View Article Online
DOI: 10.1039/D5EL00041J

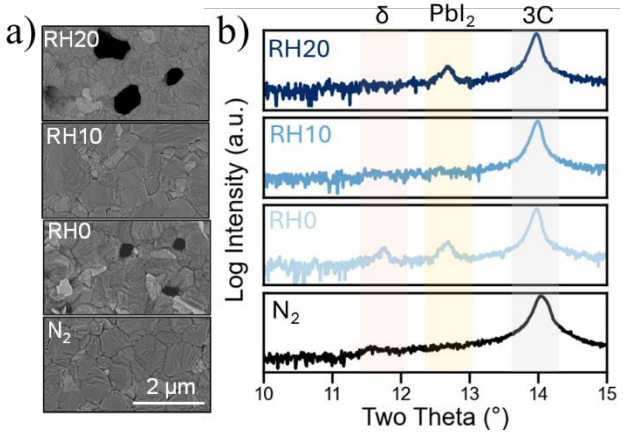

Fig. 1 (a) SEM images, scale bar 2 µm is common to all images, (b) X-ray diffraction patterns of the $FAPbI_3$ films processed under different ambient conditions: N_2, RH 0%, RH 10%, and RH 20%.

MACl additive concentration throughout film formation.[20–22] Consequently, humidity has emerged as a critical parameter in ambient processing, governing perovskite crystallization kinetics, additive volatilization, film morphology, and phase stability.[20,22]

Significant progress has been made in understanding perovskite crystallization in antisolvent-based processes under inert conditions. However, the mechanistic interplay between environmental conditions and solute–solvent interactions remain unexplored for single-step, ASF perovskite processing under ambient environment. Understanding these environment–crystallization relationships is essential for establishing precise control over film quality in manufacturing-relevant ambient environments. This control is necessary to enable scalable ASF processing routes for real-world applications.

Results and Discussion

Here, we utilize a self-volatilizing 2ME:NMP ink that doesn't require an antisolvent treatment to process 1.33 M $FAPbI_3$ with 0.2 M MACl, providing improved process control and scalability relative to traditional approaches.[13]

Morphology and X-ray diffraction

To assess the efficacy of this approach under ambient conditions, perovskite films were spin-coated and annealed under N_2 (inert), RH 0% (dry air), RH 10%, and RH 20% atmospheres. Spin coating and annealing (150 °C for 10 min) took place under the same environment in each test. The morphology and bulk structure of these films was subsequently analysed via scanning electron microscopy (SEM) and X-ray diffraction (XRD) (Fig. 1a-b). Films processed under N_2 exhibited a pinhole-free morphology with an apparent domain size of 1–2 µm. In contrast, films processed under RH 0% (dry air environment) displayed pinholes with similar grain domains. Films processed under RH 10% maintained a pinhole-free morphology with apparent domain sizes comparable to the N_2-processed films. However, at RH 20%, larger pinholes appeared along with reduced apparent domain sizes, indicating that moisture interfered with the nucleation and crystallization processes. Additionally, RH 0% films exhibited bright-contrast regions, suggesting the presence of PbI_2, which was subsequently corroborated by X-ray diffraction patterns. Fig. S1 and the semi-log scale plot of XRD (Fig. 1b) demonstrated the effect of environmental conditions on the X-ray diffraction patterns of the final films. XRD patterns showed that the N_2-processed film formed pure α-$FAPbI_3$, while films processed at RH 0% exhibited both PbI_2 and weak δ (11.9°) peaks. The RH 10% film showed phase pure pseudocubic $FAPbI_3$, but PbI_2 peaks emerged again at RH 20%. These findings corroborate the SEM observations, confirming the presence of secondary phases indicated by the bright spots observed in the RH 0% and RH 20% films. Furthermore, Williamson–Hall analysis of the X-ray diffraction patterns of $FAPbI_3$ films processed under N_2 and RH 10% revealed that films grown under low humidity conditions exhibited moderately reduced strain (Fig. S2). This suggests that humidity-controlled growth can produce higher-quality films with possibly fewer structural defects.

NMR analysis

Moisture and atmospheric oxygen in the deposition environment actively interact with perovskite precursors and influence the volatilization of organic species, thereby affecting film quality.[20] To assess the rate of MACl volatilization under ambient conditions, perovskite films processed under N_2, and RH 10% were dissolved in d^6-DMSO for ^1H-NMR analysis (Fig. S3). Films processed at RH 10% showed significantly lower signal from MA (MA-CH_3 2.373 ppm) compared to N_2-processed films, indicating that even modest humidity promotes MACl volatilization.

Photoluminescence based analysis

To further elucidate these environmental effects, we conducted photoluminescence (PL) studies on films processed under different atmospheric conditions. (Fig. 2a-b, S4). The residual MACl after annealing incorporates in $FAPbI_3$ lattice and causes a blue shift of the PL emission centre. Introducing oxygen during deposition (RH 0%) yielded emission peak positions and PL intensities comparable to those of films processed under N_2 which suggests that oxygen does not have significant influence on volatility of MACl. Increasing humidity from RH 0% to RH 20% shifted the emission peak closer to the intrinsic bulk $FAPbI_3$ band gap (~1.48 eV), suggesting enhanced volatilization of the MACl additive facilitated by environmental moisture. Films processed under N_2, RH 0%, and RH 10% exhibited comparable emission intensities. However, films processed at RH 20% showed a significant decline in emission intensity. These results suggest that RH levels exceeding 10% negatively impact film quality, which can ultimately limit or reduce open circuit voltage (V_{OC}) of devices. To further investigate the intrinsic optoelectronic quality of $FAPbI_3$ films processed under N_2 (inert) and optimal ambient condition (RH 10%), we conducted injection-dependent photoluminescence quantum yield (PLQY) measurements. (Fig. 2c). PLQY, which quantifies the fraction of radiative recombination events, provides a direct indication of the maximum attainable V_{OC}.[23,24] The quasi-Fermi level splitting was extracted from PLQY data over a series of excitation

View Article Online
DOI: 10.1039/D6EL00041J

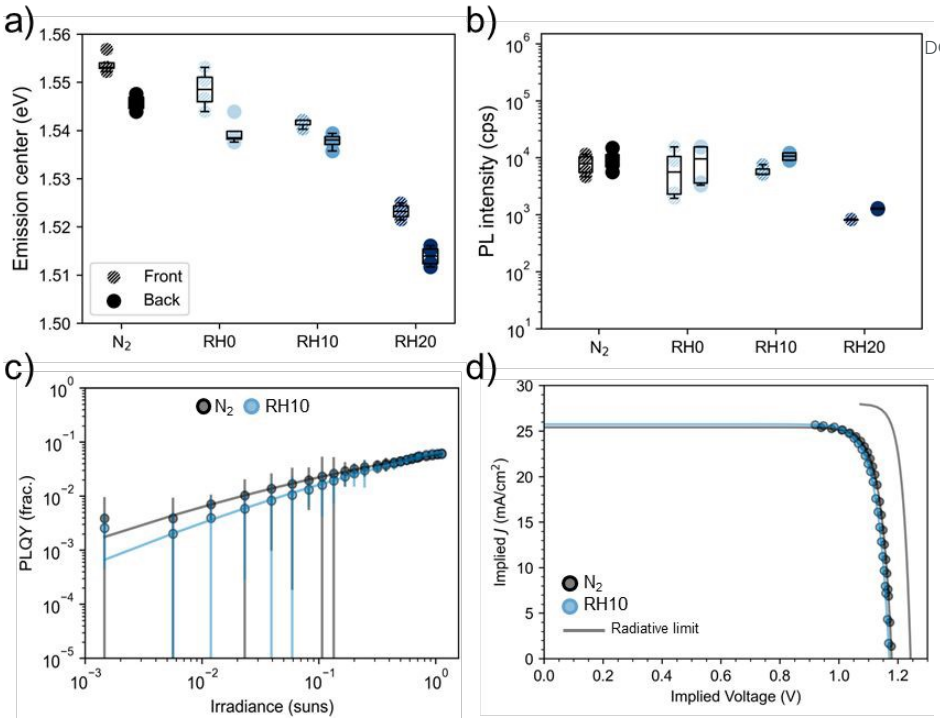

Fig. 2 (a) Emission centre and (b) photoluminescence intensity of films, and (c) light intensity dependent PLQY analysis, and (d) Implied *J-V* curves derived from PLQY measurements of films processed under different environments.

intensities, using the band gaps estimated from the emission centres of the PL spectra (Fig. 2a and Fig. S4).[25] From these values, an implied current–voltage (*iJV*) curve was plotted, providing an estimate of the theoretical efficiency limit for the perovskite absorber under ideal device conditions. For this measurement, the perovskite film was sandwiched between a hole-transporting layer (MeO-2PACz) and a passivation layer (3-aminopropyl) triethoxysilane (APTES).[14] Films processed under N_2, and RH 10% achieved the highest PLQYs under 1-sun equivalent injection of 3.1% and 3.4%, respectively. The PLQY of these films is likely limited by surface recombination velocity, as indicated by their similar values. At lower injection intensities, RH 10% films exhibited lower PLQY compared to N_2-processed films and indicating a relatively higher implied ideality factor and suggesting a lower implied fill factor. The injection-dependent PLQY curves were used to derive implied current–voltage (*iJV*) characteristics and calculate the implied power conversion efficiency (*iPCE*), which represents the maximum theoretical efficiency attainable for solar cells fabricated from these absorbers under standard terrestrial illumination. (Fig. 2d and Fig. S4). Both N_2- and RH 10%-processed films achieved an estimated *iPCE* ≈ 25.5% with iV_{OC} of ≈1.17 V, as determined from the *iJV* plots (Fig. 2d and Fig. S5). This indicates that both RH 10% and N_2 processed films have the potential to produce high performance devices. Overall, morphological, X-ray diffraction pattern, and photoluminescence analyses indicate that RH 10% provides the optimal ambient-processing condition for $FAPbI_3$ compared to RH 0% (dry air) or RH 20%.

***In situ* WAXS analysis**

To understand how moisture and oxygen affect crystallization and phase evolution during fabrication of ASF $FAPbI_3$ films from 2-ME:NMP ink, we performed *in situ* WAXS during spin-coating and annealing. In this self-volatilizing system, drying occurs in two stages: (1) spin-coating and (2) annealing, unlike conventional antisolvent-assisted methods. We examined two annealing protocols: isothermal annealing at 150 °C and ramped annealing (Fig. 3, S6-9). Ramped annealing (5 °C/20 s) was employed to improve the temporal resolution of overlapping crystallization events, enabling detection of transient intermediate phases and a clearer understanding of the preferred crystallization pathways, while normal annealing provides the conventional thermal evolution profile. *In situ* WAXS was conducted under N_2, RH 0%, RH10%, and RH 40%. The top panels in Fig. 3 and S6 show scattering intensity heat maps (logarithmic scale) depicting the evolution of diffraction intensity over time as a function of the scattering vector q (Å^{-1}) for different environments. The bottom panels trace the integrated intensities of intermediate phases over time, revealing the crystallization dynamics during spinning and the subsequent annealing.

During isothermal annealing at 150 °C, films processed at RH 0% (oxygen present) exhibited strengthened PbI_2-NMP intermediate phase intensity, while films under N_2 and RH 10% showed similar PbI_2-NMP and other FAI-PbI_2-NMP based transitional intermediate (TI) behaviour (Fig. S6). N_2-processed films underwent a rapid 2H → 3C conversion with brief 4H (q = 0.81 & 0.92 Å^{-1}) and 6H (q = 0.85 Å^{-1}) phases. Films at RH 0% displayed an intense and prolonged 4H and 6H phase, following a 2H → 4H → 6H → 3C pathway (Fig. S6). Interestingly, the crystallization pathway under RH 10% and RH 40% resembles

View Article Online
DOI: 10.1039/D5EL00041J

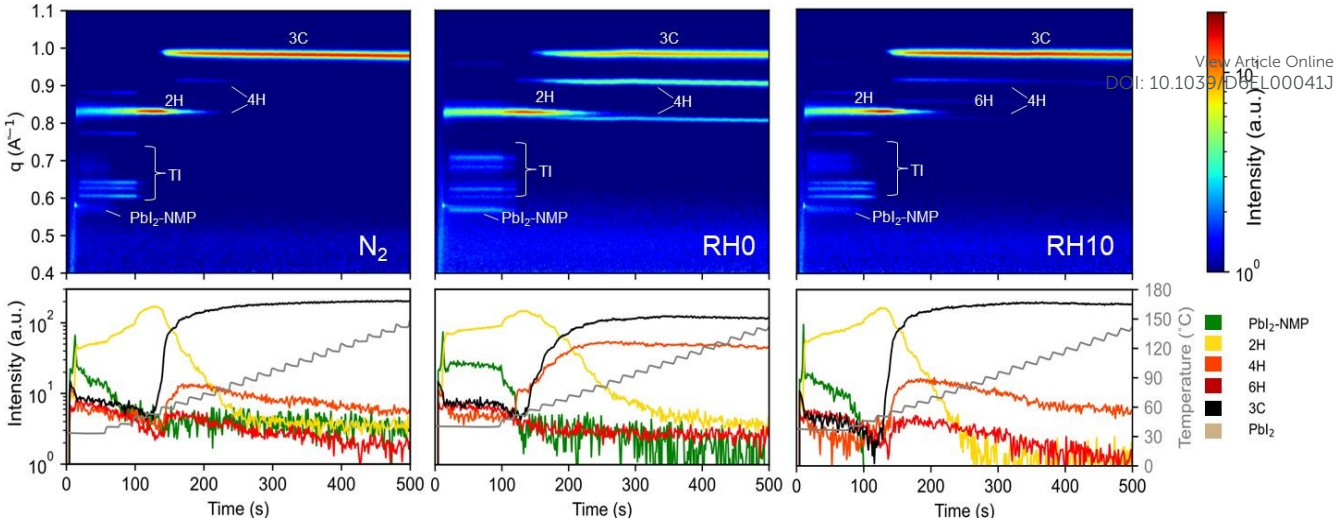

Fig. 3 Heat maps of azimuthally integrated *in situ* WAXS during the ramped annealing step of the film deposition process for films N_2, RH 0% and RH 10%, and bottom represents the time evolution of selected diffraction peaks, extracted from the corresponding diffraction data as well as the substrate temperature.

the inert condition (2H → 3C). However, the PbI_2 peak appeared under RH 40% at a later stage of the annealing due to excessive volatilization of A-site cations. Azimuthally-integrated diffraction profiles of mid-annealed and fully annealed films are shown in Fig. S7. During the mid-annealing stage, films from all environments exhibited almost phase-pure 3C, except those processed at RH 0%, which showed low-intensity peaks from additional polytypes.

Due to the rapid and environment-sensitive nature of these transformations under isothermal annealing, ramped annealing was implemented to deconvolute overlapping phases more effectively. We classify the phase evolution trajectories into two regimes: low temperature (below 50 °C) and high temperature (above 50 °C) to more precisely elucidate phase transition pathways.

Polytype evolution at low-temperature Regime (< 50 °C)

At the initial stage of drying, when the temperature is near room temperature, the films exhibit a disordered colloidal sol–gel suspension composed of perovskite precursors and solvents. Scattering is centred in the q range of 0.40–0.50 $Å^{-1}$, independent of the deposition environment (Fig. 3 and S6). A peak appears at q = 0.58 $Å^{-1}$, attributed to PbI_2–NMP complexes observed under all deposition conditions (N_2, RH 0%, RH 10% and RH 40%). These intermediates consist of PbI_2 bilayers separated by NMP solvent molecules.[13,26] Between 0.6 and 0.7 $Å^{-1}$, a distinct set of diffraction peaks emerge, referred to as TIs (Fig. 3 and S6) and these are present in N_2, RH 0%, and RH 10%. These likely arise from mixed-cation and mixed-anion frameworks coordinated with solvent or additive molecules, forming transient complexes. Notably, these features are absent under high-humidity conditions (RH 40%) (Fig. S6 and S8), suggesting that water molecules compete for PbI_2 coordination and disrupt TI formation or its stability. Additional peaks near 0.77 and 0.88 $Å^{-1}$ appear during the drying stage in films processed under N_2 and low humidity (RH 10%), likely corresponding to FAI–PbI_2–NMP complexes in the wet perovskite film.[26] These peaks are absent in films processed under RH 0% and RH 40 %. This indicates that high moisture or oxygen content can possibly destabilize these complexes.

Polytype evolution at high-temperature Regime (> 50 °C)

This annealing window encompasses the key solid-state transitions to form the 3C phase occurring across all deposition environments. As the temperature approaches 50 °C, both PbI_2–NMP complexes and TIs weaken and eventually disappear, converting into crystalline 2H $FAPbI_3$ (q = 0.83 $Å^{-1}$). The 2H phase becomes the dominant phase, though only briefly. Films processed under N_2 exhibit a direct and preferential transition from 2H → 3C, cubic phase (q = 0.98 $Å^{-1}$), with low intensity 4H (q = 0.81 & 0.92 $Å^{-1}$) and 6H (q = 0.85 $Å^{-1}$) phases present for very short period. RH 0% shows a dominant 4H phase with a preferred 2H → 4H → 3C pathway. Interestingly, when films were deposited under RH 10%, crystallization dynamics resemble the inert condition with relatively longer living 4H and 6H phases. Increasing the humidity to RH 40% caused the 4H and 6H phases to dominate throughout the entire temperature range (Fig. S8). This humidity-dependent phase evolution indicates that the preferred transition pathway under ambient conditions follows the sequence 2H → 4H → 6H → 3C, similar to polytype evolution trajectories observed in previous antisolvent-based studies of MA-FA perovskites processed under ambient environment.[27] To the best of our knowledge, our work represents the first *in situ* structural examination of single-step $FAPbI_3$ phase evolution under varied ambient conditions, revealing how moisture and oxygen modulate the crystallization pathway. Interestingly, the onset temperatures and lasting ranges of crystalline phases during annealing processing exhibit significant variation with environmental conditions (Fig. 4a). The annealing ramp was performed in 5 °C increments, and therefore the effective temperature resolution is limited to 5 °C. All reported onset temperatures should be interpreted given this uncertainty. The 3C phase emerges around 55 °C under N_2 atmosphere, approximately 60 °C at RH 0%, and 55 °C at RH 40%. Films processed under optimal humidity (RH 10%) show signs of earlier crystallization into the 3C phase, with an onset temperature around 50 °C (Fig. 4a). Nevertheless, a consistent trend in cubic phase onset temperatures is observed across conditions, where RH 10% yields the lowest onset temperature, followed by RH 40% and

View Article Online
DOI: 10.1039/D6EL00041J

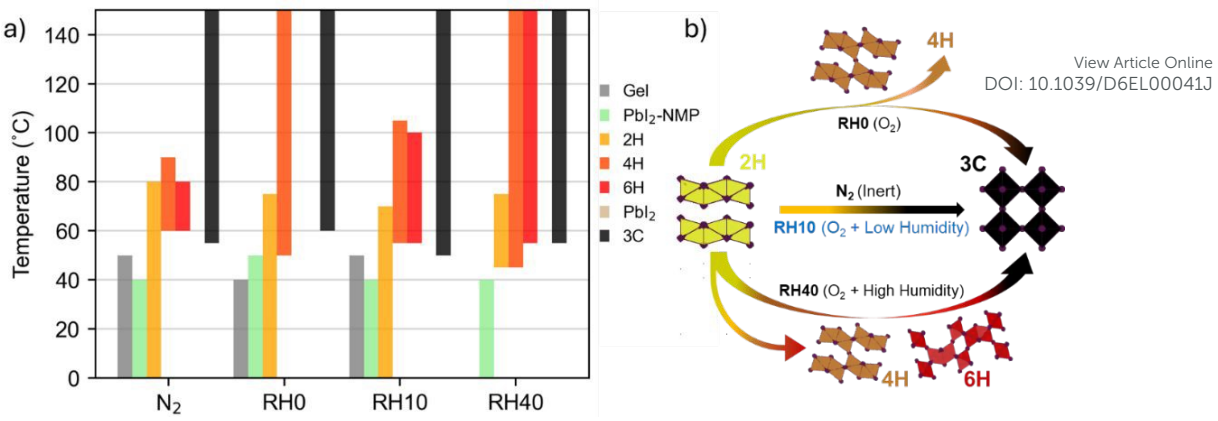

Fig 4. (a) Temperature ranges over which different phases emerge in WAXS patterns for films processed under various environmental conditions (ramped anneal) and (b) schematic representation of phase evolution and preferred crystallization pathways under each environment during ramped annealing.

N_2 at comparable values, with RH 0% showing the highest onset temperature. Fig. S9a presents the integrated GIWAXS patterns of ramped annealed films at 50 °C, revealing the early emergence of the 3C in RH 10% processed films, while films processed under other conditions remain dominated by the 2H phase with no detectable cubic phase formation.

As the temperature approaches 150 °C, the 3C phase dominates in both N_2 and RH 10% films, while RH 0% films remain rich in 4H and RH 40% films retain some 4H and 6H phases (Fig. 4a and S8). This indicates that RH 10% provides an optimal balance where moisture counteracts oxygen-induced undesired phase formation while guiding the crystallization pathway toward high-quality, phase-pure films comparable to N_2 processing. Additionally, this environment promotes earlier cubic phase formation (50 °C) and facilitates MACl volatilization. Fig. S9b shows azimuthally integrated diffraction patterns from the fully annealed films after the extended ramped protocol. Despite the prolonged ambient exposure inherent to the ramped annealing process, RH 10% samples exhibit relatively phase-pure perovskite with minimal PbI_2 impurities, comparable to N_2 processed films. In contrast, films processed at RH 0% and RH 40% contain significant quantities of undesired secondary phases. Fig. 4b schematically illustrates the preferred polytype evolution pathways under each environment, highlighting the resembling crystallization routes under N_2 and RH 10%, in contrast to the undesired phase formation under RH 0% and RH 40%.

Role of oxygen and moisture in driving crystallization

The ambient processing of $FAPbI_3$ reveals a sophisticated interplay between environmental factors and crystallization dynamics, where oxygen and moisture act as co-regulators. Oxygen has the potential to initiate a cascade of chemical transformations by oxidizing surface iodide species to iodate (IO^{3-}), which subsequently coordinates with Pb^{2+} centres to form lead (II) iodate complexes.[28] This is consistent with the observation of undesired secondary phases in diffraction and morphological analysis of RH 0% films (Fig. 1a-b). While these oxidative processes can potentially disrupt ideal crystallization pathways, they simultaneously create unique coordination environments that may influence film microstructure.

Moreover, the influence of moisture extends far beyond simple hydration effects. Characterized by its moderate donor number (D_N) between 18 kcal/mol (gas) and 33 kcal/mol (liquid) and high acceptor number of 54 kcal/mol, water exhibits selective coordination behaviour, preferentially binding to electron-deficient Pb^{2+} sites while competing with the coordinating solvent NMP (D_N = 27 kcal/mol) for binding sites.[21,26,29] Competitive binding may create a dynamic equilibrium that reshapes nucleation and crystallization kinetics, turning water from a perovskite degrader into a crystallization mediator.

Under optimized humid conditions at RH 10%, perovskite deposition yielded pinhole-free films with the lowest cubic phase transition temperature. Processing at elevated humidity levels resulted in pinhole formation and residual PbI_2 in the final films, attributable to the over-volatilization of A-site ions. This interpretation is further corroborated by the *in-situ* observations at RH 40% (Figs. S6 and S8). The diminished presence of thermally induced intermediates (TIs) and weaker PbI_2-NMP complexes at RH 40% (Fig. S6 and S8) reveal pronounced humidity-intermediate interactions at the low-temperature regime. These observations indicate that elevated moisture levels fundamentally alter the crystallization pathway, shifting it from strongly solvent-mediated routes toward moisture-assisted mechanisms.

At RH 10%, a critical balance is achieved between these competing pathways, where the combined influence of moisture and oxygen establishes a crystallization route that closely resembles that of an inert environment. In contrast, high humidity conditions (RH 40%) promote side-sharing octahedral connectivity, which favours the formation of persistent 4H and 6H polytypes, indicating a dominant oxygen and moisture interaction relative to the processing solvents.

We also speculate that H_3O^+ ions formed during moisture-assisted deprotonation of A-site cations play an active role. It is possible that they may preferentially occupy the contracted cage environments of higher order polytypes (4H and 6H) due to their small ionic radius (~100 pm), providing favourable conditions for electrostatic stabilization.[30,31] Collectively, these factors potentially influence the crystallization pathway and stabilize higher order polytypes during ambient processing.

Device performance

To further investigate the impact of environmental conditions on perovskite crystallization and device performance, solar cells were fabricated using a *p-i-n* architecture (ITO/MeO-

View Article Online
DOI: 10.1039/D6EL00041J

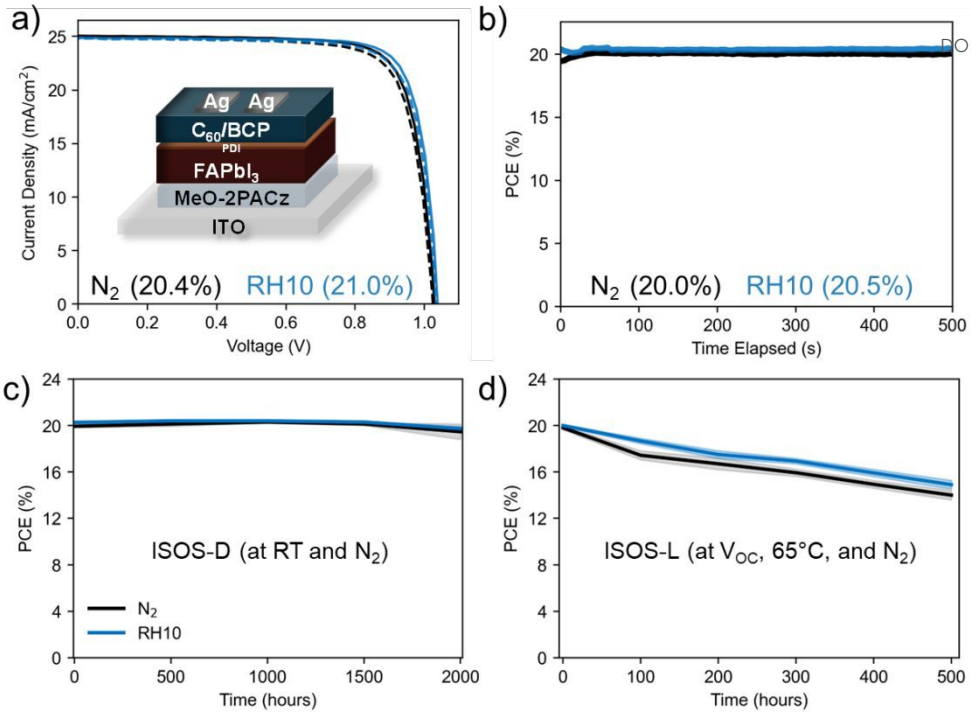

Fig. 5 (a) *J–V* characteristics (dashed = forward scan and solid line = reverse scan), (b) maximum power point (MPP) tracking, (c) ISOS-D shelf-life monitoring over 2000 hours, and (d) device stability tracking at V_{OC} over 500 hours of devices processed under N_2 and RH 10% as per ISOS-L protocol.

2PACz/$FAPbI_3$/PDI/C_{60}/BCP/Ag) following the procedures detailed in the supporting information. Fig. 5a and Fig. S10 presents the device architecture and current density-voltage (*J-V*) characteristics of devices fabricated with perovskite absorbers processed under N_2, RH 0 RH 10, RH 20%. The champion devices achieved PCEs of 20.4%, 18.6%, 21.0%, and 12.8% for perovskite films deposited under N_2, RH 0%, RH 10%, and RH 20% conditions, respectively. Devices fabricated under N_2 served as the baseline, delivering a PCE of 20.4%. Processing at RH 0% resulted in a reduced efficiency of 18.6%, indicating less favourable crystallization in presence of atmospheric oxygen. In contrast, films deposited at RH 10% achieved the highest PCE of 21.0%, reflecting a modest performance enhancement relative to N_2-processed devices, primarily driven by an improved V_{OC}. However, further increasing the humidity to RH 20% significantly degraded device performance, yielding a PCE of 12.8%, which is likely associated with suboptimal crystallization and the presence of undesirable phases and pinholes. Complete statistical distributions of all photovoltaic parameters are presented in box plot format within the supporting information (Fig. S11), while the performance metrics for the champion cells are detailed in Table S1. Benchmarking against recent literature (Fig. S12) confirms that this work represents one of the highest-performing ambient-processed *p-i-n* $FAPbI_3$ (single step) devices reported to date. Additionally, maximum power point tracking (MPPT) measurements over 500 seconds (Fig. 5b) demonstrate stable power output for both processing conditions. Interestingly, RH 10% devices (20.5%) consistently maintained marginally superior PCE values compared to their N_2-processed counterparts (20.0%) throughout the tracking period. Fig. S13 shows the external quantum efficiency (EQE) and corresponding integrated current density (J_{SC}) of the devices. The champion devices processed under N_2 (inert) and ambient conditions at RH 10% both exhibited an integrated J_{SC} of 22.5 mA/cm². In comparison, the J_{SC} obtained from the *J–V* measurement under reverse bias was 24.9 mA/cm², which is ~9% higher. Such discrepancies are commonly observed in PSCs.[32] The origin is likely multifactorial: ionic redistribution and light-soaking under continuous 1-sun illumination may enhance charge extraction; residual spectral mismatch between the broadband source and reference cell can introduce a systematic offset; and the low-intensity chopped-beam EQE conditions may not fully capture intensity-dependent charge-extraction dynamics present under 1-sun illumination. Among these, light-soaking effects are most consistent with our observations, as the discrepancy is reproducible across processing conditions. Shelf-life stability was evaluated using the ISOS-D protocol, where devices were stored in dark conditions under N_2 atmosphere (H_2O <1 ppm and O_2 <1 ppm) for 2000 hours. Both devices demonstrated excellent long-term stability, retaining >97% of their initial PCE after extended storage. The shaded regions in stability plots represent standard deviations calculated from three devices for both processing conditions.

To further assess device stability under accelerated aging conditions, we conducted ISOS-L testing at V_{OC} under 1-sun illumination at 65°C, where photoelectrochemical degradation pathways are typically more pronounced than during maximum power-point tracking of operational devices. Under this harsh testing condition, N_2-processed devices retained 70% of their initial PCE after 500 hours, while RH 10%-processed devices demonstrated improved stability, maintaining 75% of their initial efficiency with the champion device's T_{80} lifetime exceeding 400 hours (average of 3 devices). The enhanced

performance and stability of ambient-processed devices can be attributed to improved MACl volatilization and the beneficial effects of controlled moisture during crystallization, which collectively contribute to higher film quality and reduced degradation pathways. Overall, the finding that moderate humidity (RH 10%) accelerates cubic phase formation while maintaining film quality comparable to inert processing advances our understanding of perovskite crystallization dynamics, demonstrating that environmental factors can be leveraged as controllable variables to achieve scalable, efficient, and more stable device fabrication.

Conclusions

This study demonstrates that controlled ambient environments enable high-quality $FAPbI_3$ films via single-step ASF deposition. *In situ* WAXS analysis reveals a remarkable similarity between N_2 and RH 10% crystallization, both following a preferred 2H → 3C pathway with short-lived 4H and 6H polytypes. In contrast, RH 0% exhibits dominant 4H phase formation that hinders phase pure crystallization of 3C. Interestingly, low humidity (RH 10%) counteracts the detrimental impacts of oxygen alone, achieving crystallization pathway resembling N_2 with the lowest cubic phase onset temperature (50 °C). These distinct pathways originate from competitive interactions between environmental factors (oxygen and moisture) and processing solvents with iodoplumbate octahedra. Devices fabricated with perovskite processed under RH 10% demonstrate improved performance (PCE: 21.0% vs 20.4%) and enhanced operational stability compared to N_2-processed counterparts, retaining 75% efficiency after 500 hours under ISOS-L conditions versus 70% for N_2 controls. However, given the narrow humidity window involved, applying this mechanistic framework to other solvent systems, device architectures, or compositional spaces will likely require additional optimization of processing conditions. Collectively, these findings establish ambient processing as a viable alternative to inert atmosphere fabrication, providing mechanistic insights into environment-controlled crystallization while enabling scalable, cost-effective processing of high-efficiency perovskite photovoltaics using ASF process.

Acknowledgements

We acknowledge support from the U.S. Department of Energy's Office of Energy Efficiency and Renewable Energy (EERE) under Solar Energy Technologies Office (SETO) Award Number DE-EE0010503. MH also acknowledges the support from the First Solar. T.K. acknowledges support from the U.S. Department of Energy (DOE), Office of Science, Office of Basic Energy Sciences, Materials Sciences and Engineering Division under contract no. DE-AC02-05-CH11231 (D2S2 program KCD2S2). Work at the Molecular Foundry was supported by the Office of Science, Office of Basic Energy Sciences, of the U.S. Department of Energy under Contract No. DE-AC02-05CH11231. Work at the Advanced Light Source (ALS) was done at beamline 12.3.2. The ALS is a DOE Office of Science User Facility under contract no. DE-AC02-05CH11231.

Conflicts of interest

View Article Online
DOI: 10.1039/D6EL00041J

There are no conflicts to declare.

Data availability

The data supporting this article have been included as part of the ESI.†

References

1 Best Research-Cell Efficiency Chart, https://www.nrel.gov/pv/cell-efficiency.
2 C. Liu, Y. Yang, H. Chen, I. Spanopoulos, A. S. R. Bati, I. W. Gilley, J. Chen, A. Maxwell, B. Vishal, R. P. Reynolds, T. E. Wiggins, Z. Wang, C. Huang, J. Fletcher, Y. Liu, L. X. Chen, S. De Wolf, B. Chen, D. Zheng, T. J. Marks, A. Facchetti, E. H. Sargent, M. G. Kanatzidis, Two-dimensional perovskitoids enhance stability in perovskite solar cells, *Nature* 2024, ***633***, 359-364.
3 Y. Yang, H. Chen, C. Liu, J. Xu, C. Huang, C. D. Malliakas, H. Wan, A. S. R. Bati, Z. Wang, R. P. Reynolds, I. W. Gilley, S. Kitade, T. E. Wiggins, S. Zeiske, S. Suragtkhuu, M. Batmunkh, L. X. Chen, B. Chen, M. G. Kanatzidis, E. H. Sargent, Amidination of ligands for chemical and field-effect passivation stabilizes perovskite solar cells, *Science* 2024, ***386***, 898-902.
4 Z. Xiong, Q. Zhang, K. Cai, H. Zhou, Q. Song, Z. Han, S. Kang, Y. Li, Q. Jiang, X. Zhang, J. You, Homogenized chlorine distribution for >27% power conversion efficiency in perovskite solar cells, *Science* 2025, ***390***, 638-642.
5 S. Sidhik, I. Metcalf, W. Li, T. Kodalle, C. J. Dolan, M. Khalili, J. Hou, F. Mandani, A. Torma, H. Zhang, R. Garai, J. Persaud, A. Marciel, I. A. Muro Puente, G. N. M. Reddy, A. Balvanz, M. A. Alam, C. Katan, E. Tsai, D. Ginger, D. P. Fenning, M. G. Kanatzidis, C. M. Sutter-Fella, J. Even, A. D. Mohite, Two-dimensional perovskite templates for durable, efficient formamidinium perovskite solar cells, *Science* 2024, ***384***, 1227-1235.
6 M. Hossain, R. Garai, R. K. Gupta, R. N. Arunagirinathan, P. K. Iyer, Fluoroarene derivative based passivation of perovskite solar cells exhibiting excellent ambient and thermo-stability achieving efficiency >20%, *J. Mater. Chem. C* 2021, ***9***, 10406-10413.
7 Z. Li, T. R. Klein, D. H. Kim, M. Yang, J. J. Berry, M. F. A. M. Van Hest, K. Zhu, Scalable fabrication of perovskite solar cells, *Nat. Rev. Mater.* 2018, ***3***, 18017.
8 B. Parida, A. Singh, A. K. Kalathil Soopy, S. Sangaraju, M. Sundaray, S. Mishra, S. (Frank) Liu, A. Najar, Recent Developments in Upscalable Printing Techniques for Perovskite Solar Cells, *Adv. Sci.* 2022, ***9***, 2200308.
9 Y. Deng, E. Peng, Y. Shao, Z. Xiao, Q. Dong, J. Huang, Scalable fabrication of efficient organolead trihalide perovskite solar cells with doctor-bladed active layers, *Energy Environ. Sci.* 2015, ***8***, 1544-1550.
10 K. P. Goetz, Y. Vaynzof, The Challenge of Making the Same Device Twice in Perovskite Photovoltaics, *ACS Energy Lett.* 2022, ***7***, 1750-1757.
11 A. D. Taylor, Q. Sun, K. P. Goetz, Q. An, T. Schramm, Y. Hofstetter, M. Litterst, F. Paulus, Y. Vaynzof, A general approach to high-efficiency perovskite solar cells by any antisolvent, *Nat. Commun.* 2021, ***12***, 1878.
12 Q. Zhang, G. Ma, K. A. Green, K. Gollinger, J. Moore, T. Demeritte, P. C. Ray, G. A. Hill, X. Gu, S. E. Morgan, M. Feng, S. Banerjee, Q. Dai, $FAPbI_3$ Perovskite Films Prepared by Solvent Self-Volatilization for Photovoltaic Applications, *ACS Appl. Energy Mater.* 2022, ***5***, 1487-1495.

13 P. E. Marchezi, J. R. Palmer, M. Hossain, T. Kodalle, R. F. Moral, C. M. Sutter-Fella, D. P. Fenning, Polytype selection in the antisolvent-free crystallization of formamidinium lead iodide using alkylammonium chlorides, *J. Mater. Chem. A* 2025, ***13***, 16671-16680.

14 J. R. Palmer, S. Iwamoto, C. Han, C. J. Dolan, H. M. Vossler, S. P. Dunfield, D. P. Fenning, Problems with solutions: manipulating alkylammonium additive reactivity for durable high-quality perovskite films, *New J. Chem.* 2025, ***49***, 1223-1231.

15 M. Kim, G.-H. Kim, T. K. Lee, I. W. Choi, H. W. Choi, Y. Jo, Y. J. Yoon, J. W. Kim, J. Lee, D. Huh, H. Lee, S. K. Kwak, J. Y. Kim, D. S. Kim, Methylammonium Chloride Induces Intermediate Phase Stabilization for Efficient Perovskite Solar Cells, *Joule* 2019, ***3***, 2179-2192.

16 K. Odysseas Kosmatos, L. Theofylaktos, E. Giannakaki, D. Deligiannis, M. Konstantakou, T. Stergiopoulos, Methylammonium Chloride: A Key Additive for Highly Efficient, Stable, and Up-Scalable Perovskite Solar Cells, *Energy Environ. Mater.* 2019, ***2***, 79-92.

17 J. Park, J. Kim, H.-S. Yun, M. J. Paik, E. Noh, H. J. Mun, M. G. Kim, T. J. Shin, S. I. Seok, Controlled growth of perovskite layers with volatile alkylammonium chlorides, *Nature* 2023, ***616***, 724-730.

18 X. Wang, Y. Fan, L. Wang, C. Chen, Z. Li, R. Liu, H. Meng, Z. Shao, X. Du, H. Zhang, G. Cui, S. Pang, Perovskite Solution Aging: What Happened and How to Inhibit?, *Chem* 2020, ***6***, 1369-1378.

19 L. Ma, D. Guo, M. Li, C. Wang, Z. Zhou, X. Zhao, F. Zhang, Z. Ao, Z. Nie, Temperature-Dependent Thermal Decomposition Pathway of Organic–Inorganic Halide Perovskite Materials, *Chem. Mater.* 2019, ***31***, 8515-8522.

20 K. Park, S. Tan, T. Kodalle, D. Lee, M. Abdelsamie, J. Park, J. Lee, S. Jung, J. H. Ko, N. Park, C. M. Sutter-Fella, Y. Yang, J. Lee, Atmospheric Humidity Underlies Irreproducibility of Formamidinium Lead Iodide Perovskites, *Adv. Mater.* 2024, ***36***, 2307265.

21 S. Xiao, K. Zhang, S. Zheng, S. Yang, Good or evil: what is the role of water in crystallization of organometal halide perovskites?, *Nanoscale Horiz.* 2020, ***5***, 1147-1154.

22 K. Liu, Y. Luo, Y. Jin, T. Liu, Y. Liang, L. Yang, P. Song, Z. Liu, C. Tian, L. Xie, Z. Wei, Moisture-triggered fast crystallization enables efficient and stable perovskite solar cells, *Nat. Commun.* 2022, ***13***, 4891.

23 M. Stolterfoht, M. Grischek, P. Caprioglio, C. M. Wolff, E. Gutierrez-Partida, F. Peña-Camargo, D. Rothhardt, S. Zhang, M. Raoufi, J. Wolansky, M. Abdi-Jalebi, S. D. Stranks, S. Albrecht, T. Kirchartz, D. Neher, How To Quantify the Efficiency Potential of Neat Perovskite Films: Perovskite Semiconductors with an Implied Efficiency Exceeding 28%, *Adv. Mater.* 2020, ***32***, 2000080.

24 J. C. De Mello, H. F. Wittmann, R. H. Friend, An improved experimental determination of external photoluminescence quantum efficiency, An improved experimental determination of external photoluminescence quantum efficiency, *Adv. Mater.* 1997, ***9***, 230-232.

25 R. Camacho-Aguilera, Z. Han, Y. Cai, L. C. Kimerling, J. Michel, Direct band gap narrowing in highly doped Ge, *Appl. Phys. Lett.* 2013, ***102***, 152106.

26 C. Wu, D. Wang, Y. Zhang, F. Gu, G. Liu, N. Zhu, W. Luo, D. Han, X. Guo, B. Qu, S. Wang, Z. Bian, Z. Chen, L. Xiao, $FAPbI_3$ Flexible Solar Cells with a Record Efficiency of 19.38% Fabricated in Air via Ligand and Additive Synergetic Process, *Adv. Funct. Mater.* 2019, ***29***, 1902974.

27 R. Szostak, P. E. Marchezi, A. D. S. Marques, J. C. Da Silva, M. S. De Holanda, M. M. Soares, H. C. N. Tolentino, A. F. Nogueira, Exploring the formation of formamidinium-based hybrid perovskites by antisolvent methods: *in situ* GIWAXS measurements during spin coating, *Sustain. Energy Fuels* 2019, ***3***, 2287-2297.

28 J. Hidalgo, W. Kaiser, Y. An, R. Li, Z. Oh, A.-F. Castro-Méndez, D. K. LaFollette, S. Kim, B. Lai, J. Breternitz, S. Schorr, C. A. R. Perini, E. Mosconi, F. De Angelis, J.-P. Correa-Baena, Synergistic Role of Water and Oxygen Leads to Degradation in Formamidinium-Based Halide Perovskites, *J. Am. Chem. Soc.* 2023, **145**, 24549−24557.

29 P. Zhou, Y. Xiang, K. Liu, Understanding and applying the donor number of electrolytes in lithium metal batteries, *Energy Environ. Sci.* 2024, ***17***, 8057.

30 S. Sobczak, A. M. Fidelli, J.-L. Do, G. P. Demopoulos, A. Moores, T. Friščić, A. Katrusiak, High-pressure observation of elusive iodoplumbic acid in different hydronium-hydrate solid forms, *Inorg. Chem. Front.* 2024, ***11***, 735-744.

31 M. Daub, H. Hillebrecht, On the Demystification of "$HPbI_3$" and the Peculiarities of the Non-innocent Solvents H_2O and DMF, *Z. Für Anorg. Allg. Chem.* 2018, ***644***, 1393-1400.

32 M. Saliba, E. Unger, L. Etgar, J. Luo, T. J. Jacobsson, A systematic discrepancy between the short circuit current and the integrated quantum efficiency in perovskite solar cells, *Nat. Commun.* 2023, ***14***, 5445.

View Article Online
DOI: 10.1039/D6EL00041J

Data availability

The data supporting this article have been included as part of the ESI.†